POLITECNICO DI TORINO
Repository ISTITUZIONALE

Challenges in shallow target reconstruction by 3D elastic full-waveform inversion - Which initial model?

(Article begins on next page)

08 November 2022

Challenges in shallow target reconstruction by 3D elastic full-waveform inversion — Which initial model?

Daniela Teodor[1], Cesare Comina[2], Farbod Khosro Anjom[3], Romain Brossier[4], Laura Valentina Socco[3], and Jean Virieux[4]

ABSTRACT

Elastic full-waveform inversion (FWI) is a powerful tool for high-resolution subsurface multiparameter characterization. However, 3D FWI applied to land data for near-surface applications is particularly challenging because the seismograms are dominated by highly energetic, dispersive, and complex-scattered surface waves (SWs). In these conditions, a successful deterministic FWI scheme requires an accurate initial model. Our study, primarily focused on field data analysis for 3D applications, aims at enhancing the resolution in the imaging of complex shallow targets, by integrating devoted SW analysis techniques with a 3D spectral-element-based elastic FWI. From dispersion curves, extracted from seismic data recorded over a sharp-interface shallow target, we build different initial S-wave (V_S) and P-wave (V_P) velocity models (laterally homogeneous and laterally variable), using a specific data transform. Starting from these models, we carry out 3D FWI tests on synthetic and field data, using a relatively straightforward inversion scheme. The field data processing before FWI consists of band-pass filtering and muting of noisy traces. During FWI, a weighting function is applied to the far-offset traces. We test 2D and 3D acquisition layouts, with different positions of the sources and variable offsets. The 3D FWI workflow enriches the overall content of the initial models, allowing a reliable reconstruction of the shallow target, especially when using laterally variable initial models. Moreover, a 3D acquisition layout guarantees a better reconstruction of the target's shape and lateral extension. In addition, the integration of model-oriented (preliminary monoparametric FWI) and data-oriented (time windowing) strategies into the main optimization scheme has produced further improvement of the FWI results.

INTRODUCTION

The accurate reconstruction of sharp-interface shallow targets, from land acquisition data, is controlled by the nontrivial wavefield behavior when interacting with them. Particularly, the proper reconstruction of low-velocity localized shallow heterogeneities is important for accurate imaging of the velocity structure at greater depth. The effectiveness of commonly used tools for near-surface characterization is partially limited in this respect.

First-arrival traveltime tomography, often used to retrieve the P-wave velocity (V_P) variation, is not sensitive to embedded low-velocity horizons. For small-offset acquisitions, the arrival time picking process may be complicated due to the difficulty in separating various phases. Several surface-wave (SW) analysis and inversion techniques can be adopted to retrieve the S-wave velocity (V_S) variation, using processing workflows based on windowing and wavefield transform to extract and invert local dispersion curves (DCs). However, the reconstructed V_S variation may not be accurate enough in the presence of sharp lateral transitions, given the locally 1D assumption of SW methods. Compared with near-surface phase-oriented imaging techniques, full-waveform inversion (FWI), based on waveform analysis, overcomes these limitations while ensuring a theoretical resolution equal to half of the local propagating wavelength (Virieux and Operto, 2009).

FWI also allows for the simultaneous reconstruction of multiple parameters (e.g., V_P, V_S, mass density, and attenuation factor) providing a more detailed site characterization.

FWI is defined as a nonlinear iterative data fitting procedure, based on numerical solution of the seismic wave equation (Virieux and Operto, 2009; Fichtner, 2011). After the introduction of FWI by Lailly (1983) and Tarantola (1984), successful applications have been performed in the time and frequency domains. FWI is under continuous development, supported by the simultaneous evolution of the parallel computing architectures. Nevertheless, one of its bottlenecks is still the high computational cost. For this reason, most of the FWI applications, especially for marine data, are performed using the acoustic approximation (e.g., Warner et al., 2013; Operto et al., 2015). The 2D elastic approximation is also used for exploration-scale marine and land data sets (e.g. Bretaudeau et al., 2013; Vigh et al., 2014; Borisov et al., 2020), but the time-domain 3D elastic or viscoelastic FWI examples are still rare in the literature (e.g., Epanomeritakis et al., 2008; Borisov and Singh, 2015; Fathi et al., 2015; Trinh et al., 2019). As far as the FWI application for shallow structures imaging is concerned, most of the studies are based on the 2D approximation (e.g., Brossier et al., 2009; Romdhane et al., 2011; Tran and McVay, 2012; Bretaudeau et al., 2013; Dou and Ajo-Franklin, 2014; Groos et al., 2014, 2017; Masoni et al., 2014; Schäfer et al., 2014; Amrouche and Yamanaka, 2015; Köhn et al., 2016; Nuber et al., 2016; Pan et al., 2016, 2019; Krampe et al., 2019; Wang et al., 2019). The full-3D FWI applications for near-surface characterization are less common nowadays (Butzer et al., 2013; Fathi et al., 2016; Borisov et al., 2018; Nguyen and Tran, 2018; Irnaka et al., 2019; Smith et al., 2019; Tran et al., 2019), and most of them focus on the reconstruction of predominantly depth-dependent distributions of the subsurface physical parameters.

Although FWI is mainly driven by body waves for upper-crust imaging (Sirgue et al., 2010; Warner et al., 2013), data from shallow acquisitions are dominated by SWs. For near-surface reconstruction, elastic or viscoelastic propagation must be considered. However, one of the main challenges of the multiparameter inversion is related to the different sensitivity of the algorithm with respect to each parameter class. Another challenge is the increase of computational cost and dimensionality of the inverse problem when considering viscoelastic propagation. Therefore, a linearized formulation based on quasi-Newton methods is the most widespread technique, given its computational efficiency. Another challenging aspect is related to the commonly used least-squares (L_2) objective function, which contains many local minima (Brossier et al., 2010). Consequently, an accurate initial model is required for proper convergence.

One of the strategies aimed to mitigate the FWIs nonlinearity follows a multiscale and multiresolution hierarchical approach (Bunks et al., 1995; Fichtner et al., 2013), starting the inversion from low frequencies (long wavelengths) and gradually incorporating the higher frequencies (short wavelengths). An alternative is the layer-stripping procedure: the model reconstruction proceeds hierarchically from the shallow part to the bottom, whereas the offset range is gradually increased as a function of the penetration depth (Virieux and Operto, 2009; Shi et al., 2015; Masoni et al., 2016): This is especially true for SWs with a specific medium probing related to the depth dependence of the eigenmodes.

FWI applications for shallow targets reconstruction are overly sensitive to the initial model, particularly in the presence of flat topographies. This is mainly due to the complex structure of the wavefield, with highly energetic and forward-scattered phases combined altogether. Therefore, dedicated strategies are required for the correct definition of the initial model. An accurate initial model can be retrieved with global inversion strategies, essentially used for 2D geometries (Tran and Hiltunen, 2012a, 2012b; Xing and Mazzotti, 2019a, 2019b). Nevertheless, for 3D applications, the significant computation resources required by the probabilistic techniques limit their use. In this framework, SW analysis may be a more efficient approach for building accurate V_S and V_P initial models. However, only the V_S initial model is commonly retrieved, whereas the V_P model is usually inferred from V_S by assuming a constant Poisson's ratio (e.g., Nguyen and Tran, 2018; Tran et al., 2019). Nonetheless, recent studies (Socco and Comina, 2017; Socco et al., 2017) have introduced a method, based on the concept of SW skin depth, that allows estimating the V_S and V_P models. Khosro Anjom et al. (2019) propose a DC clustering algorithm that efficiently organizes data subsets for mitigating the impacts of strong lateral variations. A specific data transform allows building the V_S and V_P models over complex shallow environments. This procedure has been applied to synthetic (Teodor et al., 2018) and field (Khosro Anjom et al., 2019) data, resulting in a good initial waveform matching. Furthermore, Teodor et al. (2019) present a few preliminary results of FWI tests on synthetic data, starting from initial models built from DC analysis and using a 2D acquisition geometry.

In this study, we integrate V_S and V_P models, retrieved using the above DC analysis techniques, into a spectral-element-based elastic 3D FWI workflow. The method, used for the construction of the initial model from SWs, allows characterizing high lateral contrasts and provides V_S and V_P models. We carry out 3D FWI, on synthetic and field data, using 2D and 3D acquisition schemes. Our purpose is assessing the DCs analysis method's robustness for building initial models for elastic FWI. We keep the FWI workflow relatively simple and focus our analysis on the initial model's effectiveness. However, we incorporate an offset variable weighting function to the conventional FWI algorithm, to guarantee more accurate data fitting for the far-offset traces.

We briefly present the SW analysis method and the 3D FWI tool. Henceforth, we apply the 3D FWI workflow on the various initial models (laterally homogeneous and laterally heterogeneous) retrieved from DC analysis, for synthetic and field data, and we highlight the main challenges that arise. The potential benefits of adopting various FWI strategies are also discussed.

METHODS

Our methodology for the characterization of complex shallow targets relies on the integration of velocity models retrieved from DC analysis into an elastic 3D FWI workflow. The DC analysis step provides initial V_S and V_P models for FWI, from a devoted SW analysis procedure. These models are then used as a first guess in a spectral-element-based elastic 3D FWI scheme.

SW analysis procedure

The initial model building follows the method introduced by Socco et al. (2017) and Socco and Comina (2017). A detailed description, integrating a clustering algorithm and the total variation regularization, is presented in Khosro Anjom et al. (2019). A synthesis of the DC analysis workflow is given in Teodor et al. (2018,

2019). In summary, the procedure comprises the following steps:

1) The DCs are extracted from seismic data using a Gaussian windowing approach (Bergamo et al., 2012).
2) A clustering algorithm divides the DCs into homogeneous sets, according to metric criteria based on the Euclidean distance between adjacent DCs (Khosro Anjom et al., 2019).
3) A reference DC is selected inside each cluster and inverted to a reference V_S profile using a Monte Carlo approach (Socco and Boiero, 2008).
4) The reference V_S is transformed into a depth-continuous time-average V_S profile, according to equation 1:

$$v_{Sz} = \frac{\sum_n h_i}{\sum_n \frac{h_i}{v_{Si}}},$$ (1)

where h_i and v_{Si} are the thickness and the shear velocity of the ith layer, respectively.

5) Starting from the reference DC and the corresponding time-average V_S profile, a characteristic relation between the SW wavelength and the investigation depth is inferred (W/D relationship).
6) All DCs inside each cluster are directly transformed into time-average V_S profiles by using this W/D relationship.
7) For each reference model, inside each cluster, the W/D relationship's sensitivity to Poisson's ratio variation is used to estimate the apparent Poisson's ratio (Socco and Comina, 2017).
8) The apparent Poisson's ratio is used to transform time-average V_S profiles into time-average V_P profiles.
9) The time-average velocities are converted to interval velocities by using total variation regularization on a Dix-type formula (Khosro Anjom et al., 2019).
10) The depth-dependent continuous interval-velocity profiles along the seismic line are interpolated to 2D models and then converted to 3D volumes. The continuous velocity profile is well suited for the FWI procedure, avoiding sharp interfaces.

FWI algorithm

The 3D SEM46 FWI tool (Spectral Element for Seismic Imaging in eXploration) (Trinh et al., 2019) has been used for all numerical tests in this work. The implementation relies on nonoverlapping hexahedra spectral-element architecture, in which a deformed Cartesian-based mesh is coupled with high-order functions. Each element is projected to a 3D Gauss-Lobatto-Legendre (GLL) domain, discretized into a set of $(n + 1)^3$ points, where n is the interpolation order used to accurately model the viscoelastic wave propagation with approximately five or six GLL nodes per shortest wavelength (Trinh et al., 2019). A second-order explicit Newmark scheme is implemented for time integration to compute the displacement field at each time step (Komatitsch and Tromp, 1999; Trinh et al., 2019).

The viscoelastic wave propagation is modeled using second-order partial differential equations. The attenuation mechanism assumes constant quality factors (Q_P and Q_S), represented by standard linear solids (SLSs), each one effective over limited frequency bands (Yang et al., 2016a). The attenuation coefficients are explicitly incorporated into the wave equation, and a memory-variable vector is associated

with each SLS (Trinh et al., 2019). A compressed boundary implementation is used for memory mitigation (Yang et al., 2016c; Trinh et al., 2019). Moreover, an efficient strategy for stable recovery of the incident field (needed for construction of the misfit gradient) is implemented (Yang et al., 2016b; Trinh et al., 2019).

The linearized inversion relies on various local optimization methods, gathered by the Seiscope optimization toolbox (Métivier and Brossier, 2016), which is embedded in the SEM46 code through a reverse-communication interface. All Newton-type strategies are based on the same line-search algorithm that satisfies the Wolfe conditions (Nocedal and Wright, 2006; Trinh et al., 2019). The gradient of the least-squares misfit function concerning the model parameters $\mathbf{m}$ is computed in the time domain using the adjoint state approach (Plessix, 2006). For example, the gradient with respect to the elastic tensor's coefficients $\mathbf{C}_{ij}$ is the zero-lag crosscorrelation between the incident and the adjoint strain wavefields (Plessix, 2006; Vigh et al., 2014):

$$\frac{\partial_\chi(\mathbf{m})}{\partial C_{ij}} = \left(\bar{\boldsymbol{\varepsilon}}, \frac{\partial \mathbf{C}}{\partial C_{ij}} \boldsymbol{\varepsilon} \right)_{\Omega, t},$$ (2)

where $\mathbf{C}_{ij}$ is the Voigt matrix (6×6) containing the coefficients of the elastic tensor, $\bar{\boldsymbol{\varepsilon}}$ is the adjoint strain field, and $\boldsymbol{\varepsilon}$ is the incident strain field. The gradient for the density is computed through the zero-lag crosscorrelation between the adjoint displacement field and the incident acceleration field (Trinh et al., 2019):

$$\frac{\partial_\chi(\mathbf{m})}{\partial \rho} = \left(\bar{\mathbf{u}}, \frac{\partial^2}{\partial t^2} \mathbf{u} \right)_{\Omega, t},$$ (3)

The gradient with respect to any desirable parameter α (e.g., seismic velocity, anisotropic parameter, and impedance) can be retrieved by the chain rule, using the density ρ and the stiffness coefficient $\mathbf{C}_{ij}$ (Trinh et al., 2019):

$$\frac{\partial \chi(\mathbf{m})}{\partial \alpha} = \sum_{i=1}^{6} \sum_{i=1}^{6} \frac{\partial \chi}{\partial \mathbf{C}_{ij}} \frac{\partial \mathbf{C}_{ij}}{\partial \alpha} + \frac{\partial \chi}{\partial \rho} \frac{\partial \rho}{\partial \alpha}.$$ (4)

A gradient smoothing by a 3D anisotropic and nonstationary Bessel filter is efficiently performed on the mesh of the spectral element method (SEM) modeling (Trinh et al., 2017). This filter has an arbitrary local orientation, using three Euler angles and spatially variable coherent lengths along these three specific directions. The inversion algorithm allows performing multiple sequential gradient smoothing runs. For example, a double application of the Bessel filter has been proven to be an accurate approximation of a Laplace filter (Trinh et al., 2017).

DATA SETS AND INITIAL MODELS

Data sets

The field data sets correspond to 2D and 3D seismic acquisitions, carried out in the experimental area of the Italian National Research Council (CNR) located in Turin, Italy (Khosro Anjom et al., 2019). The site is characterized by a complex-shaped loose-sand body (Figure 1a) surrounded by more compact sediments (gravelly sands and gravels). The maximum width of the sand target is 5×5 m in its shallower part and 2×2 m at its maximum depth (which is 2.5 m).

For 2D and 3D acquisitions, an 8 kg sledgehammer was the adopted vertical point source, generating a signal with a central frequency of approximately 60 Hz. The S/N has been improved by stacking from 8 to 10 shots for each source point.

For the 2D acquisition, 11 seismograms were recorded along the seismic line R1–R72 (Figure 1b), which gathers 72 vertical receivers (4.5 Hz) evenly spaced every 0.3 m (Figure 1c). The 3D acquisition (Figure 1d) gathers four seismic lines, perpendicular to the R1–R72 line. Each seismic line contains 18 vertical receivers (4.5 Hz) evenly spaced every 0.5 m. The shotpoints, activated every

0.75 m, are perpendicular to the receiver lines. The distance between two adjacent receiver lines is 2.5 m, whereas the distance between the shot "lines" is 2 m. An additional eight common-shot gathers (highlighted by the green circles in Figure 1d) were also recorded, outside both extremities of each seismic line, with an in-line distance of 2 m from the corresponding first receiver.

Before applying the entire workflow to the field data set, we carried out some tests over a synthetic data set that realistically reproduces the site characteristics. Figure 2 shows the reference 3D model used in these synthetic tests. The model is characterized by a 3D layered structure with an embedded low-velocity target. The model is extended beyond the acquisition area to avoid boundary artifacts during numerical simulations. We used the SEM46 code to simulate viscoelastic wave propagation with a constant density value (equal to 1800 kg/m^3, a typical value for unconsolidated sediments) and attenuation models determined from a rheological expression (Hauksson and Shearer, 2006), slightly modified to fit the characteristics of a shallow environment. In these expressions, the Q_S is computed from V_S ($Q_S = 0.15 \cdot V_S$) and the Q_P is related to Q_S ($Q_P = 1.5 \cdot Q_S$). In particular, Q_S varies between 12 (in the sand target) and 74 (at the maximum depth), whereas the corresponding minimum and maximum values for Q_P are 18 and 110, respectively.

For the computation mesh, we honored the stability condition considering at least five GLL points per shortest wavelength and using an element size of 0.3 m for the 3D grid. According to the Courant-Friedrichs-Lewy time stability criterion, a sampling time step of 1.4e-05 s was required, for a total duration of the simulation of 0.412 s. The source time function is a Ricker wavelet, with a central frequency of 60 Hz, similar to the dominant frequency of the field data. We applied a free-surface boundary at the top of the model and absorbing boundaries at the other edges.

Figure 3a shows an example of a field common-shot gather corresponding to the 2D acquisition (shot 1), whereas Figure 3b shows an example of simulated reference data, belonging to the 2D acquisition, for the same shot position as the one displayed in Figure 3a. The effect of the low-velocity target is clearly evidenced by the presence of scattered and dispersive SWs in the seismograms. In addition, the body and SW amplitudes are attenuated by the sand body.

Initial models derived from DC analysis

From the reference synthetic data set, we extracted nine DCs, corresponding to nine Gaussian windows along the seismic line R1–R72 (Teodor et al., 2018). For the field data application, we also considered the four DCs extracted from the shot gathers located in external positions with respect to the four lines of the 3D
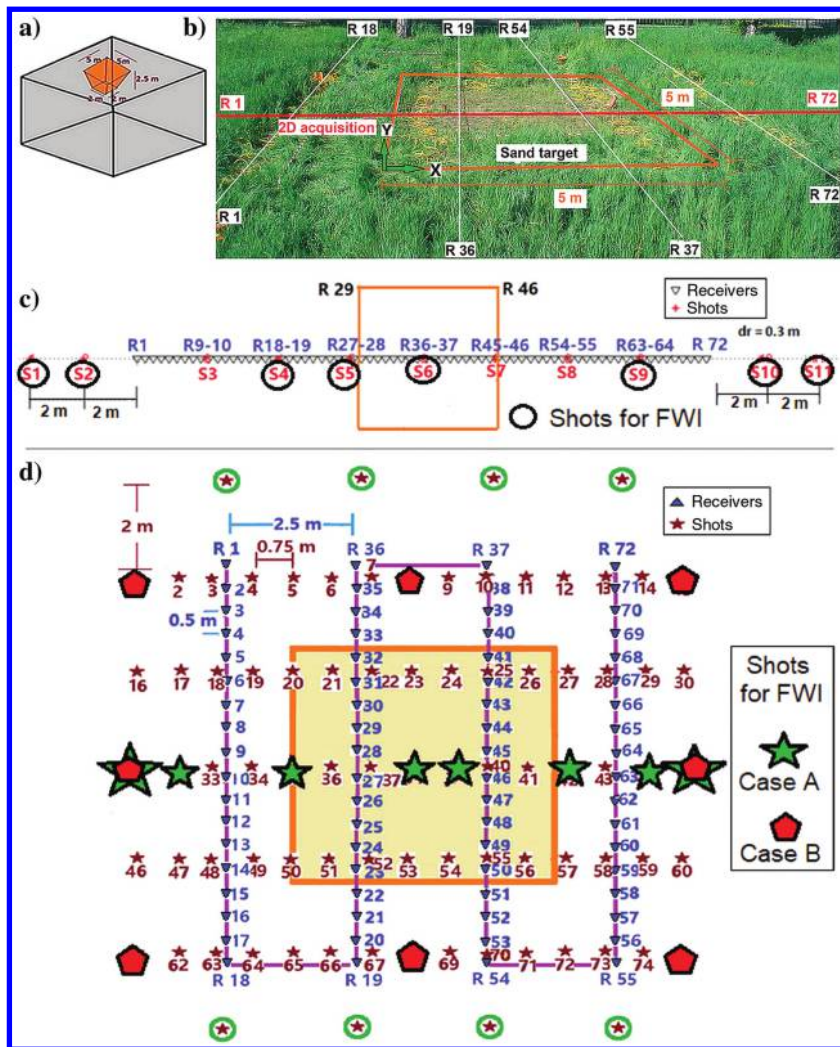

Figure 1. Overview of the site characteristics and field acquisition. (a) Simplified geometry of the sand target in the experimental site. (b) Survey geometry of the 2D and 3D acquisition: line R1–R72 gathers the receivers of the 2D acquisition, whereas lines R1–R18, R19–R36, R37–R54, and R55–R72 contain the receivers of the 3D acquisition. (c) Source and receiver location for the 2D acquisition: the receivers (R) located in the vicinity of the shots are indicated with numbers from 1 to 72. The shots (S) are labeled with numbers from 1 to 11. The shots used for FWI are highlighted with the black circles. The position of the sand target is marked by the orange rectangle. (d) The source and receiver location for the 3D acquisition. The receivers are indicated with blue inverted triangles, whereas the shots are labeled with dark-red stars. The orange rectangle indicates the target location. The shots marked with green circles have been additionally considered (together with the 2D acquisition's shot) in the DC analysis step. The green stars and red polygons indicate the positions of the shots for 3D FWI experiments, identified as case A and case B in this paper.

acquisition (Figure 1d), to enrich the lateral resolution (Khosro Anjom et al., 2019). We converted the DCs into velocity profiles, by using the data transform on a single reference DC for the single-DC analysis and a clustering algorithm together with the data transform for the full-DC analysis. Finally, we laterally interpolated the V_P and V_S 1D profiles to construct 2D models. These models were extended laterally and in depth to avoid boundary artifacts during the numerical simulations. The lateral extension was based on invariance, whereas for the depth extension, we exploited the low-frequency information provided by the DCs. Therefore, no information coming from the reference models was used for the extension process. For FWI, as required by the SEM46 code, we converted the 2D models to 3D volumes by symmetrically replicating the zx-vertical sections in the y-direction and reproducing the 3D extension of the target. In the y-direction, beyond the horizontal extension of the low-velocity target, the model is characterized by a vertically layered and laterally invariant structure (as in the x-direction, far from the sand target).

FULL-WAVEFORM INVERSION

We started with a relatively simple FWI workflow and gradually increased its complexity when necessary. By simple FWI workflow we mean a workflow that does not contain any model- or data-oriented strategy (time windowing, frequency sweeping, etc.). Data preprocessing consists of a fifth-order Butterworth filter application with corner frequencies of 3 and 40 Hz. We also muted some noisy traces at near offsets (0.3–0.6 m). According to the space-sampling criterion for SEM modeling and considering the maximum frequency of 40 Hz, we used an element size of 1 m, equal in all directions of the 3D mesh. The time stability criterion required a sampling step of 4.8e-05 s, leading to 8600 time steps for a total duration of the simulation of 0.4128 s.

We considered eight shots for the gradient computation and inversion labeled 1, 2, 4, 5, 6, 9, 10, and 11 (Figure 1c) for the 2D acquisition and 31, 32, 35, 38, 39, 42, 44, 45 and 1, 8, 15, 31, 45, 61, 68, 75, respectively (Figure 1d), for the 3D acquisitions. The source-time function was estimated using the deconvolution technique (Pratt et al., 1999), for each acquisition scheme, after applying the 3–40 Hz band-pass filter. Because we did not identify significant cycle-skipping issues in the initial model (Teodor et al., 2018; Khosro Anjom et al., 2019), we performed all FWI iterations in the full frequency band of 3–40 Hz and used the same source time functions, related to each acquisition design, for all iterations.

No data normalization was applied before or during the inversion because the 3D propagation ensures a good agreement in amplitude variation with offset (AVO) between the field and modeled data. The source wavelet estimated from the field data handles the amplitude difference between the real and modeled wavefields. During FWI, we applied an offset-variable data weighting that acts on the field and simulated data to enhance the far-offset residuals in the gradient computation and, therefore, guarantee a similar contribution for each receiver over the entire seismograms. Because almost all of the energy remains trapped inside the low-velocity target (Figure 4a), we enhanced the amplitude of the far-offset traces, up to the same magnitude of the near-offset ones (Figure 4b), to increase their

contribution in the optimization process. The various FWI experiments proved that the offset weighting strategy is particularly important when using a 2D acquisition design (and long offsets). Conversely, it is less effective when using a 3D acquisition scheme (and shorter offsets), although it still guarantees a lower data misfit after FWI.

We also used bound constraints for the V_P and V_S parameters to avoid a possible nonphysical model update during inversion. In particular, we fixed the maximum V_P (1000 m/s) and minimum V_S (60 m/s) and set depth-variable constraints for the minimum V_P and maximum V_S, inferred from the initial models by applying a vertical gradient to a scaling factor based on the depth-by-depth ratio between V_P and V_S. We inverted simultaneously for V_P and V_S and kept the density constant (1800 kg/m^3) to focus the analysis on the velocity model update and avoid a possible trade-off between the primary and secondary parameters during FWI. For the same reason, we used constant values also for the attenuation coefficients
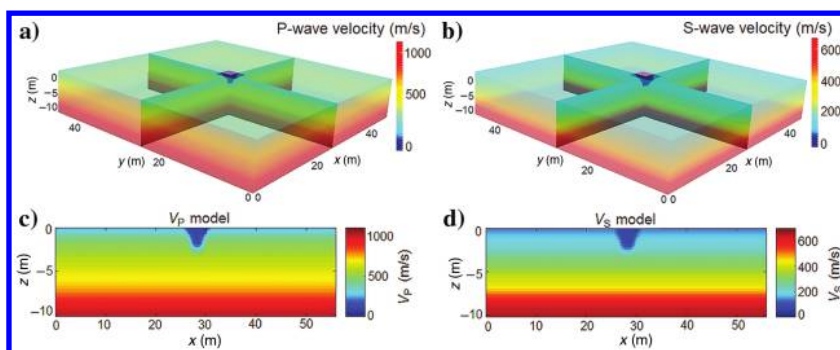
Figure 2. Synthetic 3D model used to generate the reference data set. (a) P-wave velocity model, (b) S-wave velocity model, and (c and d) 2D vertical sections (crossing the low-velocity target) of the 3D models.
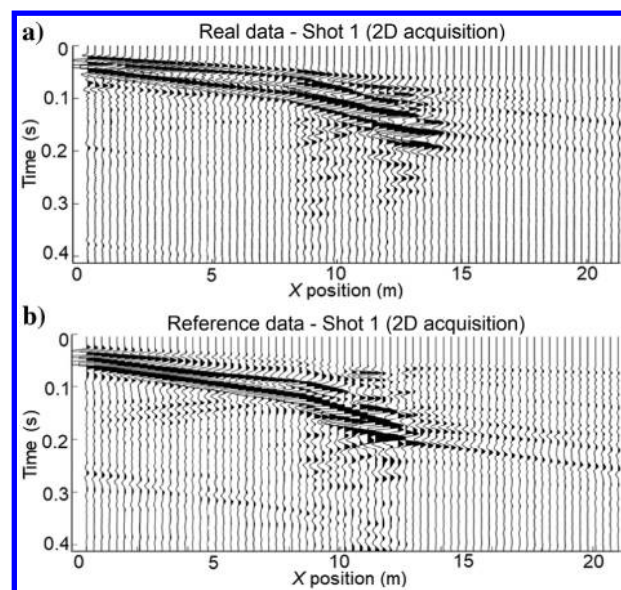
Figure 3. Example of vertical component (a) field data and (b) synthetic data simulated from the reference model. The entire seismograms are normalized by the absolute corresponding maximum value for display purposes.

in the forward modeling step of FWI and kept these parameters fixed during inversion ($Q_P = Q_S = 40$).

We did not apply preconditioning or regularization, other than gradient smoothing. We observed small-wavelength artifacts in
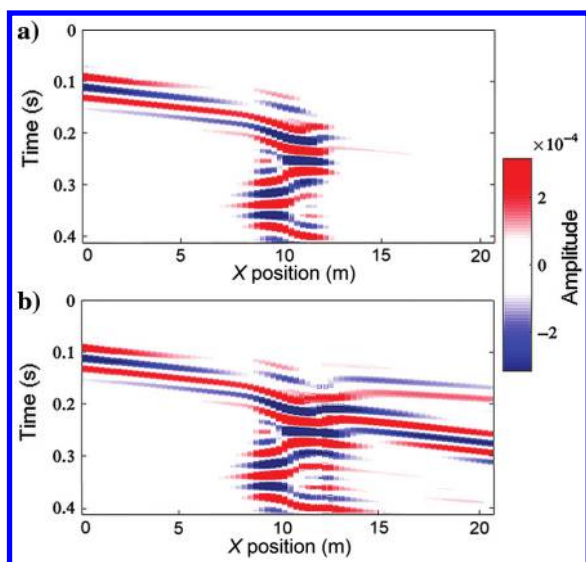

Figure 4. Reference synthetic data (shot 1). (a) Not normalized seismogram, before applying the offset-variable weighting function and (b) after the application of the weighting function to the far-offset traces.
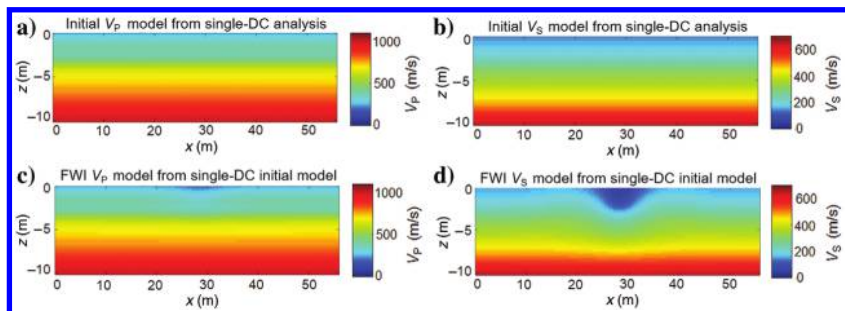

Figure 5. Vertical 2D sections of the 3D initial and final models of the synthetic application, crossing the low-velocity target. (a and b) Initial V_P and V_S models, respectively, retrieved from single-DC analysis, and (c and d) V_P and V_S models, respectively, obtained after FWI.
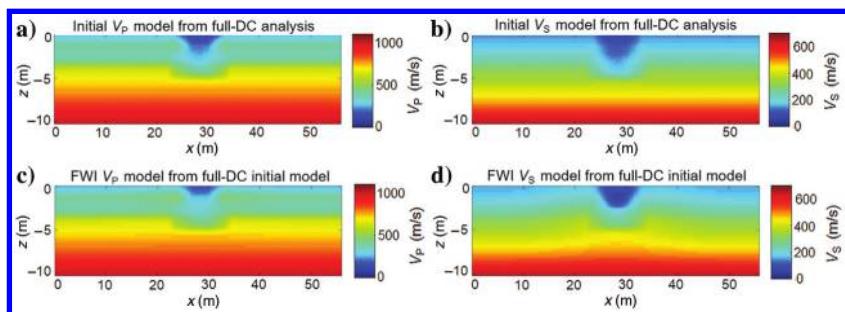
Figure 6. Vertical 2D sections of the 3D initial and final models of the synthetic application, crossing the low velocity target. (a and b) Initial V_P and V_S models, respectively, retrieved from the full-DC analysis, and (c and d) V_P and V_S models, respectively, obtained after FWI.

the gradient, not in agreement with the FWI resolution allowed by the frequency content of the data. Thus, to control the wavenumber content of the updated models according to the resolution limits, we smoothed the gradient through a double application of an anisotropic Bessel filter (Trinh et al., 2017). The choice for the filter's shape is based on the mesh dimension (1 m) for the vertical direction, wavelength resolution ($\lambda/2$) for the inline direction, and acquisition design (2D or 3D) for the crossline direction. Then, the filter has the following lengths in the z-, x-, and y-directions: 1.5, 5, and 12 m for the 2D acquisition and 1.5, 5, and 5 m for the 3D acquisition.

The optimization scheme is based on the quasi-Newton limited memory-Broyden-Fletcher-Goldfarb-Shanno method. The inversion stopped when the value of the misfit function no longer decreased for more than two consecutive iterations. Using 128 cores, the necessary time for the first gradient computation was approximately 11 min, whereas each FWI test took approximately 12 h. The convergence criterion was reached after 6–25 iterations. The FWI tests started from the two different initial V_P and V_S models extracted from DC: laterally homogeneous and laterally variable. Hereafter, we call the first configuration the "single-DC case" and the second configuration the "full-DC case." The models obtained after FWI are referred to as the "final" models, whereas the data computed from these models are called "inverted" data.

Synthetic results for the 2D acquisition design

Figure 5a and 5b shows the initial 2D models that resulted from the single-DC analysis; they do not contain any information related to the low-velocity target. Figure 5c and 5d shows the corresponding V_P and V_S models after FWI. The target is reconstructed with low resolution for the V_S model, whereas the V_P model is not significantly modified after inversion. Figure 6a and 6b shows the initial models resulted from the full-DC analysis; they contain the low-velocity target, although the resolution is still low. Figure 6c and 6d shows the corresponding models after FWI. These results show a better resolution compared with the results of the single-DC case and, again, V_S is updated more than V_P.

In Figure 7, we show the normalized model misfit (computed as normalized difference between reference and initial or final model), before and after FWI, for the single-DC case. Although V_S improves (Figure 7d), the V_P improvement is limited (Figure 7c). Figure 7d reveals an overall low misfit value at the target's position after FWI, except for some boundary areas where V_S is underestimated. In Figure 8, we show the normalized model misfit, before and after FWI, for the full-DC case. The term V_S is more accurately reconstructed (Figure 8d) compared to the final V_S of the single-DC case. The misfit value in correspondence to the target is low. The target's boundaries are better defined, although a very slight underestimation in velocity is still present. The term V_P is better recovered (Figure 8c) than in the single-DC case, although

the V_P model misfit in correspondence to the target is still high after inversion.

Figure 9a and 9b shows the trace-by-trace data fitting comparison for far offsets, before and after FWI, respectively, corresponding to the full-DC case. The trace-by-trace normalization was applied only for display purposes. The fitting is already accurate before inversion for the near offsets. We can notice a data fitting improvement after FWI, especially in correspondence to the target. Still, the back-scattered phases close to the target's boundaries, and some far-offset arrivals, are not properly fitted. In Figure 9c and 9d, we show an example of data fitting comparison for near offsets, before and after FWI, corresponding to the full-DC case. As observed, all arrivals are accurately fitted after FWI.

Field data application using a 2D acquisition design

For the field data set, we applied the same FWI workflow used in the synthetic case. In Figure 10a and 10b, we show the initial velocity models obtained from the single-DC analysis. Figure 10c and 10d displays the corresponding V_P and the V_S models after FWI. The target becomes distinguishable in the V_P and V_S models, although V_S is reconstructed better than V_P. The normalized difference between the final and initial models related to the single-DC case indicates a velocity decrease in correspondence to the target, for V_P (Figure 10e) and V_S (Figure 10f), although the V_S resolution is higher than the resolution of V_P.

Figure 11a and 11b corresponds to the velocity models obtained via the full-DC analysis. Notice that the maximum depth and the lateral boundaries of the low-velocity target are correctly recovered. In Figure 11c and 11d, we show the corresponding V_P and V_S models after FWI. The target is already well defined in the initial models, and no significant improvement is obtained after the 40 Hz inversion. The artifacts below the low-velocity target, produced by the 1D to 2D interpolation in the initial model, are not reduced by the FWI process. In contrast, the normalized difference between the final and initial model for the full-DC case reveals an improvement at the target, for V_P (Figure 12e) and V_S (Figure 11f). The model is not modified outside the target after FWI because the layered structure of the initial model from DC analysis already correctly reproduces the velocity variation of the site.

In Figure 12a and 12b, we show the data fitting comparison, before and after FWI, for the single-DC case. The misfit improvement is clear at the sand target's position. Nevertheless, some far-offset arrivals require greater improvement.

Figure 12c and 12d shows the data fitting comparison, before and after FWI, for the full-DC case. The initial model provides a good fitting at the target position; consequently, FWI does not bring
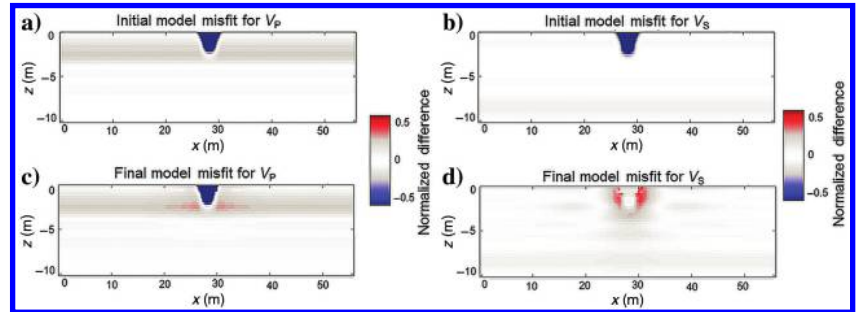

Figure 7. Model misfit for the single-DC synthetic case, computed as the normalized difference: [(reference model – initial or final model)/reference model]. (a) Initial model misfit for V_P. (b) Initial model misfit for V_S. (c) Model misfit for V_P after inversion. (d) Model misfit for V_S after inversion.
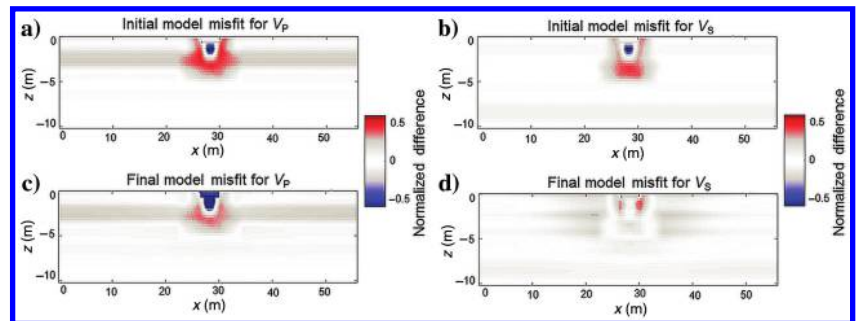

Figure 8. Model misfit for the full-DC synthetic case. (a) Initial model misfit for V_P. (b) Initial model misfit for V_S. (c) Model misfit for V_P after inversion. (d) Model misfit for V_S after inversion.
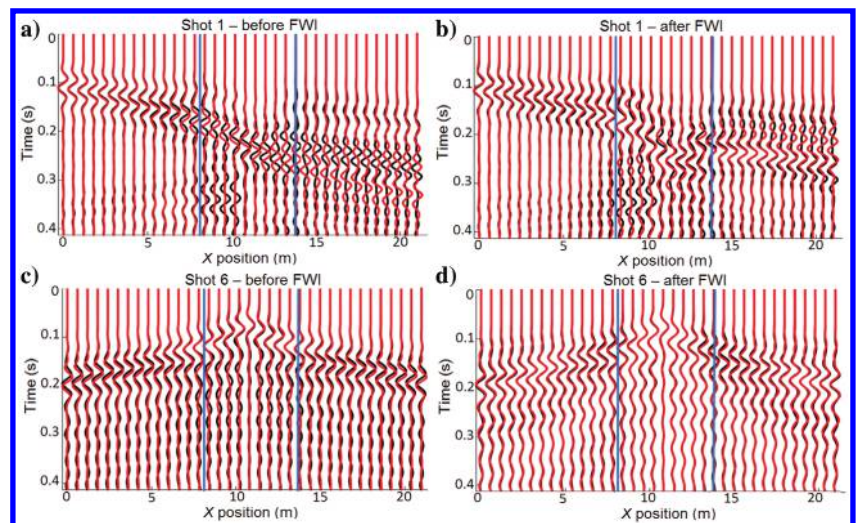

Figure 9. Data fitting comparison (a and c) before and (b and d) after FWI, for the full-DC case. The reference data are displayed in black, whereas the corresponding synthetic traces, computed for the initial and final models, are displayed in red. The blue lines indicate the location of the low-velocity target. The seismograms are trace-by-trace normalized for display purposes only. For better visualization, the data are undersampled: only the traces corresponding to one over two receivers are displayed.

significant changes. However, the backscattered phases may require more elaborate FWI strategies to be reproduced more accurately.

In Figure 13, we show the difference between the final models of the single- and full-DC cases. Figure 13a reveals an overestimation of V_P in correspondence to the target for the former case compared to the latter case, whereas the difference between the final single-DC V_S model and the final full-DC V_S model is small (Figure 13b).

Synthetic results for the 3D acquisition layout

We present here the results of two FWI cases having a different distribution of the sources (Figure 1d). In case A, the sources are activated along a line crossing the low-velocity target. In case B, the sources are placed around the low-velocity target, at a certain distance from its boundaries. In both cases, we used the initial models from the full-DC analysis.

In Figure 14a and 14c, we show 2D vertical sections of the 3D final models for case A, whereas in Figure 14b and 14d, we show

Figure 10. Vertical 2D sections of the 3D initial and final models, crossing the low-velocity target, for the field data application: (a and b) V_P and V_S models, respectively, retrieved from single-DC analysis, (c and d) final V_P and V_S models, respectively, and (e and f) normalized V_P and V_S differences, respectively, between the final and initial models.

Figure 11. Vertical 2D sections of the 3D initial and final models, crossing the low-velocity target, for the field data application: (a and b) V_P and V_S models, respectively, obtained from the full-DC analysis, (c and d) final V_P and V_S models, respectively, and (e and f) normalized V_P and V_S differences, respectively, between the final and initial models.

2D vertical sections of the 3D final models for case B. As observed, the target's shape is reconstructed with higher resolution for the acquisition configuration used in case B, compared with that of case A. Figure 14e and 14f shows the final 3D V_S models for cases A and B, respectively. We notice a better reconstruction of the horizontal target's extension, in the x-direction, for case B. The target's extension in the y-direction is known before FWI.

With the 3D acquisition design that provided the best results (case B), we performed another FWI test, using the initial model from the single-DC analysis. Figure 15a and 15b shows 2D sections of the final 3D models. As expected, the target is not recovered in the V_P model (Figure 15a), whereas its reconstruction is relatively accurate in the V_S model (Figure 15b); nevertheless, some artifacts are present in the final V_S model. In Figure 15c and 15d, showing a detail of the shallow part of the V_P and V_S models, one can notice how the target's horizontal extension is not defined in the final V_P model, whereas it is accurately reconstructed in the final V_S model, in the x- and y-directions, even if the initial model is laterally homogeneous.

Field data application using a 3D acquisition design

We performed FWI on field data, using the acquisition configuration of case B and the single- and full-DC-based initial models. Figure 16 shows 2D sections of the 3D final models, obtained when using the initial models retrieved from single-DC analysis (Figure 16a and 16c), and the initial models built by full-DC analysis (Figure 16b and 16d). For the single-DC case, the target is not recovered in the V_P model, whereas its reconstruction in the V_S model is relatively accurate, except for some artifacts present at intermediate depth. For the full-DC case, the resolution improves after FWI, but mainly for the V_S model. For the single-DC case (Figure 16e) and the full-DC (Figure 16f) experiments, the horizontal extension of the target is accurately determined at a shallow depth after FWI.

Figure 17a and 17b shows the waveform fitting comparison, before and after FWI, for the single-DC case. The overall fitting improves after inversion, especially for those events traveling through the sand body, as the velocity field is correctly recovered. Figure 17c and 17d shows the waveform fitting comparison, before and after FWI, for the full-DC case. Although the fitting is already accurate in the initial configuration, a slight improvement is noted after FWI, especially for the events traveling through the low-velocity target. The fitting improvement is proven by the crosscorrelation lag, whose value averaged over the entire seismogram decreases from 11.2 to 10.6 ms for the single-DC case and from 9.9 to 6.2 ms for the full-DC case. Exclusively considering the events traveling through the sand body, the average crosscorrelation lag value decreases from 2.2 to 1.8 ms for the single-DC case and from 2.0 to 1.1 ms for the full-DC
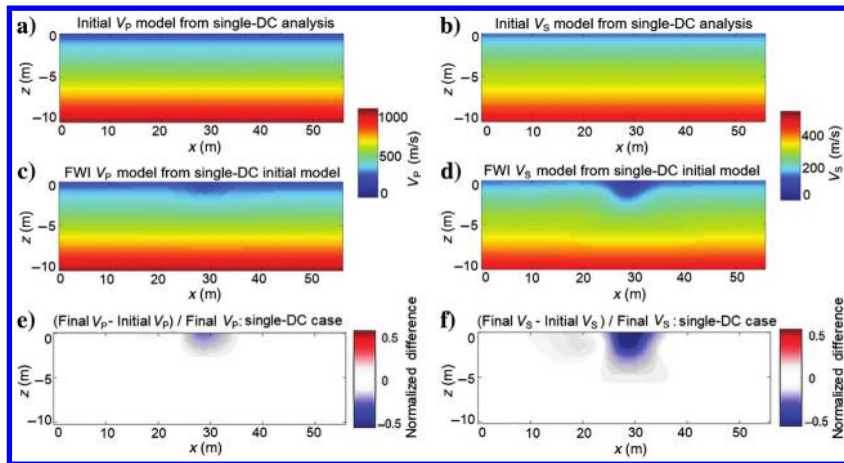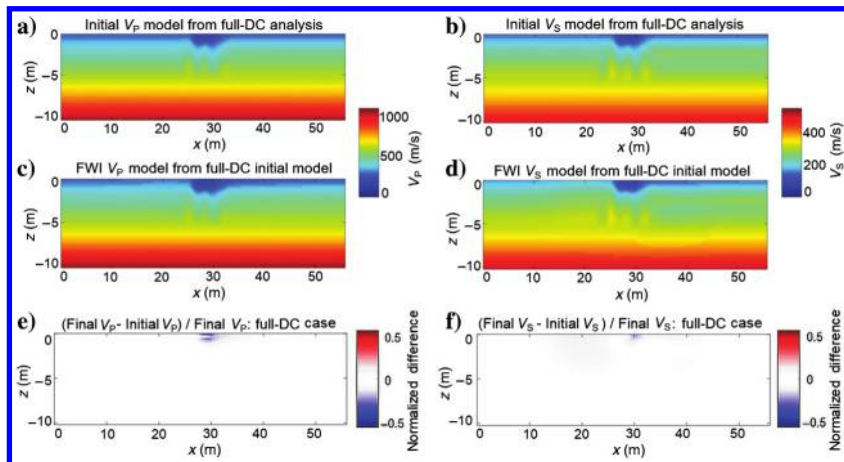
case. The phases scattered from the target boundaries bring the main contribution to the increase of the crosscorrelation lag value.

DISCUSSION

One of the main findings of this study is related to the importance of the initial model accuracy when using FWI for reconstructing heterogeneous shallow targets. Accordingly, an observation arising from this study is the different FWI convergence behavior when the initial model is laterally variable or homogeneous. In Figure 18a and 18b, we show the evolution of the L_2 misfit function with respect to the iterations for the 2D and 3D acquisitions (case B), respectively. The results show that a laterally variable initial model, derived from the analysis of the entire set of DCs, guarantees a better convergence (e.g., the green curve in Figure 18a and 18b). The final values of the normalized misfit for the full-DC case (0.64 for field data and 0.12 for the synthetic data in 2D acquisition design; 0.26 for field data and 0.21 for synthetic data in 3D acquisition design) are relatively similar to the ones obtained by other 3D FWI tests, performed for shallow environments at the same scale (e.g., Tran et al., 2019).

For the 2D acquisition design, the L_2 misfit related to the field data full-DC case (Figure 18a, the red curve) decreases less because the initial model is already accurate and such an acquisition layout does not help for further improvement. In the previous section, we have seen how the initial models from the field-data full-DC analysis are not significantly updated after FWI, whereas the initial models (particularly V_S) from the single-DC analysis are correctly updated. These observations suggest that an acceptable reconstruction of V_S could be obtained from a simple FWI workflow (starting with a laterally homogeneous initial model) and from the proposed full-DC analysis, without passing through the inversion step (Figure 13b). However, results characterized by a better resolution are expected from a higher frequency FWI workflow. Moreover, when using a 3D acquisition scheme with a 3D distribution of the shots around the target, a better convergence is also obtained for the field data application (Figure 18b, the red curve).

Besides the above main findings, the presented results highlight additional challenges in the shallow targets reconstruction related to the complex wavefield propagation. In the following, we present possible strategies that might improve FWI's performance in this context.

V_P update mitigation and model reconstructions at greater depths

Results from multiparameter FWI studies using near-surface seismic data show that V_S is predominantly updated over V_P. This fact is justified by the physics of SW propagation, more sensitive to the shear properties, and by the intrinsic lower V_P resolution (i.e., larger wavelengths due to the higher velocity values).

Another important observation is related to the predominantly shallow model update. Because the gradient is dominated by SWs, velocity updates are constrained by the penetration depth of these events. The integration of data from passive seismic acquisitions
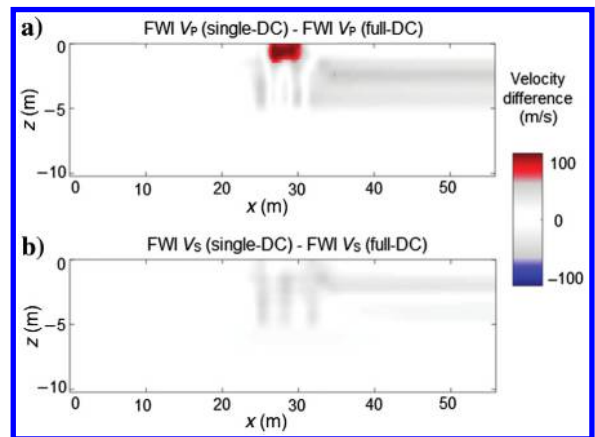
Figure 13. Vertical 2D sections, crossing the low-velocity target, of the 3D velocity difference between the final models for the single- and full-DC cases, for the field data application: (a) V_P difference and (b) V_S difference.
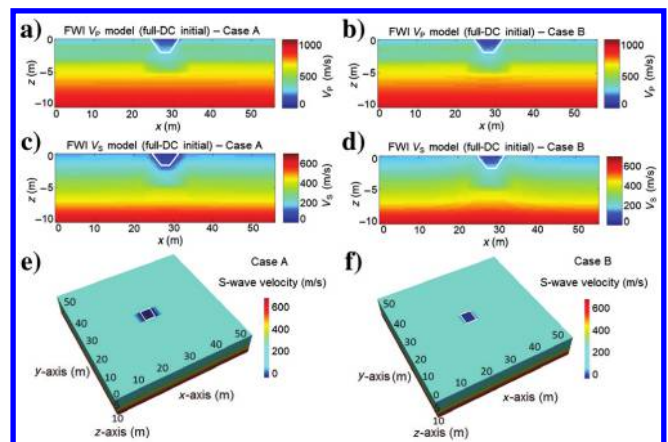
Figure 14. Vertical sections, crossing the low-velocity target, and 3D final models for the synthetic application using a 3D acquisition scheme: (a) V_P and (c) V_S models, respectively, obtained after FWI when using the initial models from the full-DC analysis and the acquisition scheme of case A: (b) V_P and (d) V_S models, respectively, obtained after FWI when using the initial models from the full-DC analysis and the acquisition scheme corresponding to case B; and (e and f) final 3D S-wave velocity models (zero depth detail) obtained for cases A and B, respectively.
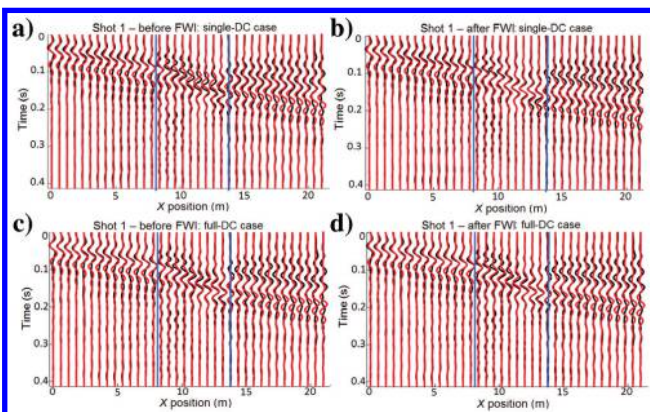

Figure 12. Field data waveform comparison for far offsets, corresponding to the single-DC case, (a) before and (b) after FWI, and to the full-DC case, (c) before and (d) after FWI. The figure notations are the same as in Figure 9.

(which better constrain the low-frequency content of the DCs), or depth preconditioning of the gradient, could be efficient strategies for enabling a deeper model reconstruction. Another strategy could be data windowing, i.e., a preliminary inversion using the P-wave arrivals, and later incorporation of the entire wavefield. This strategy should help for better reconstruction of the V_P model because FWI would efficiently exploit the body waves in the early stage of the inversion. We made synthetic data tests following this strategy, using the initial models from full-DC analysis and a 2D acquisition design. Figure 19a and 19b shows the V_P and V_S models, respectively, obtained after the preliminary inversion step, whereas Figure 19c and 19d shows the corresponding models obtained after FWI. One can notice an improvement of the target's resolution in the V_S model after the second inversion step, ensured by the introduction of SWs. The V_P model's improvement is still not substantial due to the very weak body waves (BWs) amplitude.
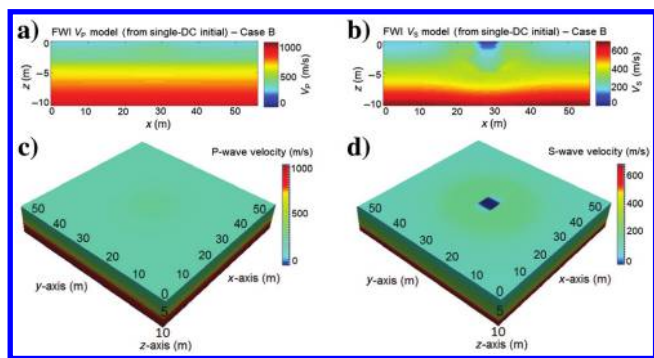
Figure 15. (a and b) Vertical 2D section of the 3D V_P and V_S models, respectively, obtained after FWI (the single-DC case) on synthetic data, using a 3D acquisition design (case B). (c and d) Detail of the shallow part (zero depth detail) of the final V_P and V_S models, respectively.
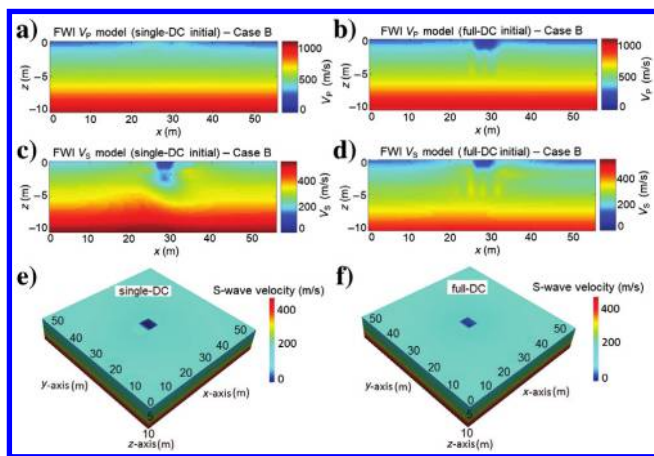

Figure 16. Vertical 2D sections, crossing the low-velocity target, and 3D final models for the field data application using a 3D acquisition scheme: (a and c) V_P and V_S models, respectively, obtained after FWI when using the initial model from the single-DC analysis and the acquisition scheme corresponding to case B; (b and d) V_P and V_S models, respectively, obtained after FWI when using the initial model from the full-DC analysis and the acquisition scheme corresponding to case B; and (e and f) 3D S-wave velocity models obtained from FWI on field data, for the single- and full-DC cases, respectively (zero depth detail).

Regardless, the effectiveness of the time-windowing strategy is case-dependent, and it may work differently for a data set characterized by BWs with higher amplitudes (e.g., Athanasopoulos et al.,
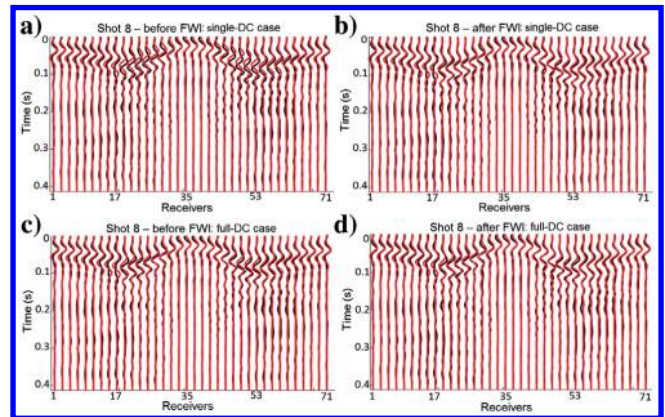

Figure 17. Example of a data fitting comparison for a common-shot gather corresponding to the 3D acquisition, field data application, for the single-DC case (a) before and (b) after FWI, and for the full-DC case (c) before and (d) after FWI. The figure notations are the same as in Figure 9.
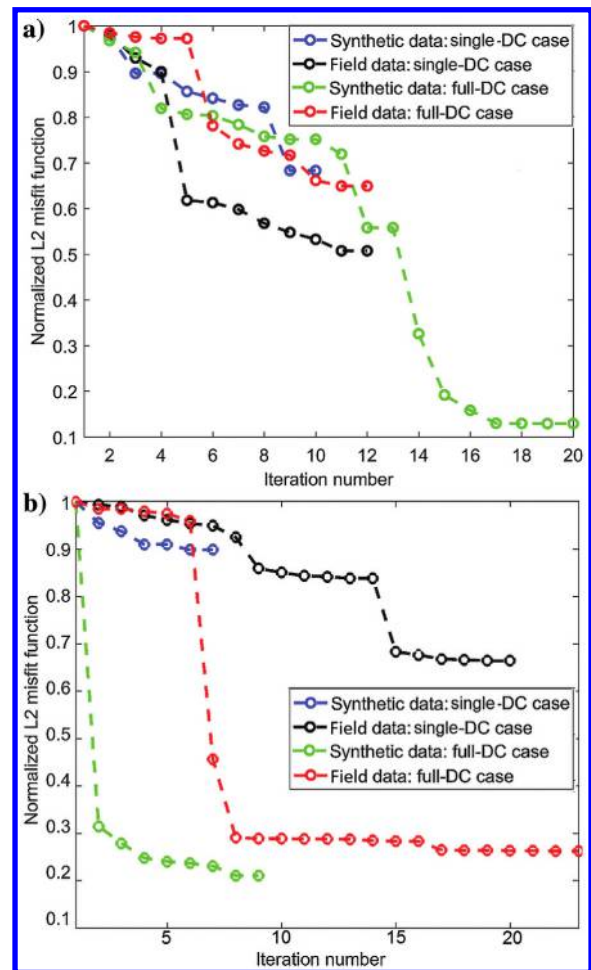

Figure 18. Normalized data misfit versus iteration number for (a) FWI experiments based on a 2D acquisition design and (b) a 3D acquisition design (case B).

2018; He et al., 2018; Trinh et al., 2018, 2019). However, the time-windowing strategy efficiently ensures a better data fitting for the far-offset arrivals. This fact is evident when comparing the final data fitting obtained when FWI is performed directly for the entire time window (Figure 20a) with that obtained when an early arrival waveform inversion step precedes FWI (Figure 20b).

Using a 3D acquisition layout also leads to the improvement of the V_P model after FWI, probably due to the better illumination guaranteed by the phases reflected from the 3D target boundaries. This is validated in Figure 21, which displays the normalized differences between the reference and final models for different cases. Figure 21b corresponds to a 2D acquisition layout and a time-windowing strategy. Figure 21c corresponds to a 3D acquisition layout and no windowing strategy. Better reconstruction of the V_P model is observed in Figure 21c.

Better approach for the initial V_P model building?

However, for a data set dominated by SWs, because the V_P model is not significantly updated when using a FWI without selecting events, an accurate initial V_P model is necessary. An alternative approach to build an initial V_P model is the first-arrival traveltime tomography. We performed numerical experiments using this approach and obtained accurate results for the high-velocity layers (Figure 22). As observed, there is an overestimation in V_P at the deepest region (Figure 21c). In contrast, the V_P field is considerably underestimated in the shallow part of the model, down to 2.0–2.5 m depth (Figure 22b and 22c). These results suggest that, in the presence of low-velocity areas, the DC analysis may provide a better initial V_P model for FWI compared with the first-arrival traveltime tomography.

Data-oriented and model-oriented FWI strategies

Additional data- and model-oriented strategies can be incorporated in the FWI workflow to control the proper evolution of the optimization process according to the wavelength resolution. Filtering (low- to high-frequency sweeping) and tapering are possible key paths for better convergence. As far as the model strategies are concerned, the SWs sensitivity to the shear properties can be exploited to improve the initial V_S model through a preliminary monoparametric (V_S) FWI step. We experimented with such a

Figure 19. Vertical 2D sections (crossing the target's center) of the 3D velocity models, synthetic application: (a) V_P model obtained after the first time-windowing step, (b) V_S obtained after the first time-windowing step, (c) final V_P model, and (d) final V_S model.
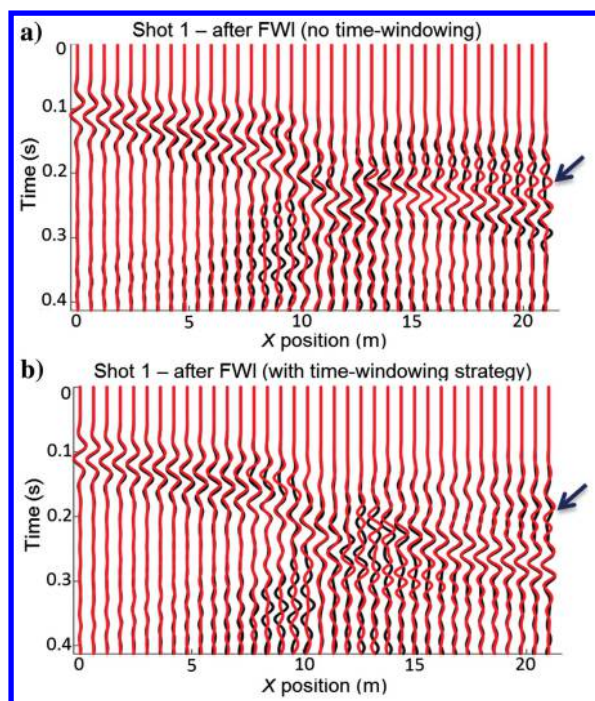

Figure 20. Example of data fitting comparison for far offset, synthetic application, (a) for the case with no time windowing strategy and (b) a two-step FWI, based on a time-windowing strategy. Notations are the same as in Figure 9.
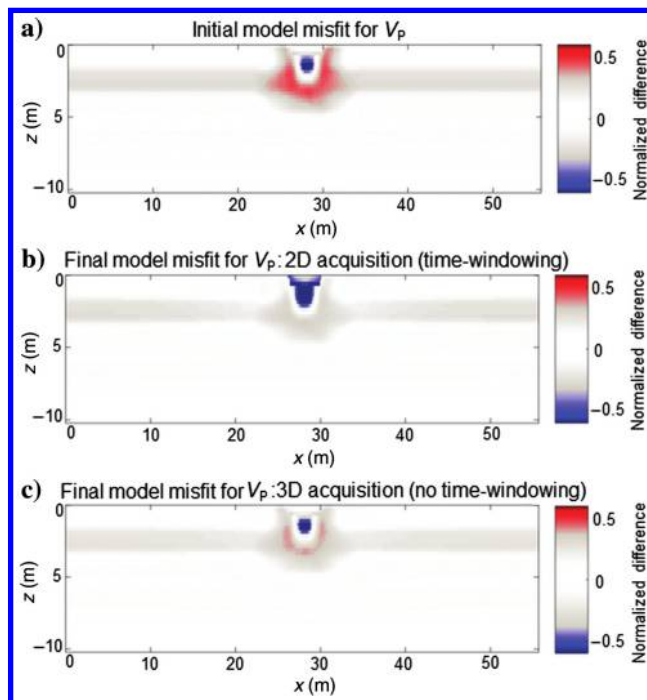

Figure 21. Model misfit for V_P computed as (reference model – FWI model)/reference model. (a) Initial model misfit for V_P. (b) Final model misfit for V_P when using a 2D acquisition scheme for FWI and a time-windowing strategy. (c) Final misfit for V_P when using a 3D acquisition scheme for FWI and no time-windowing strategy.
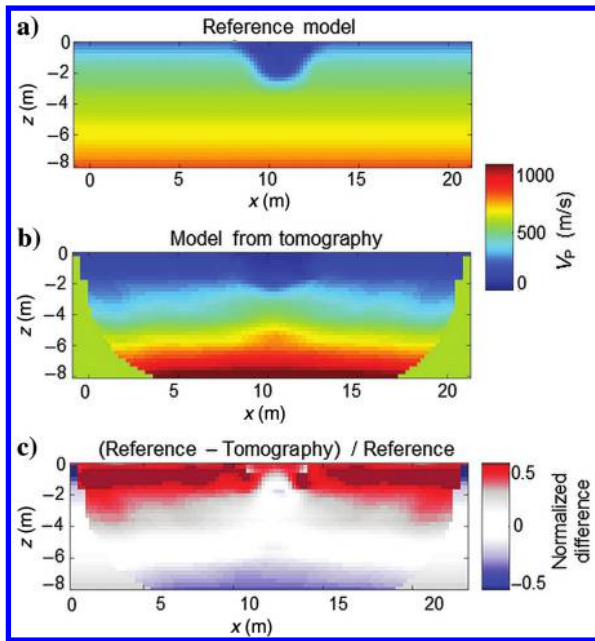
Figure 22. (a) Reference synthetic V_P model. (b) The V_P model obtained from the first-arrival traveltime tomography. (c) Model misfit computed as the normalized difference between the reference model and the model obtained from first-arrival traveltime tomography.
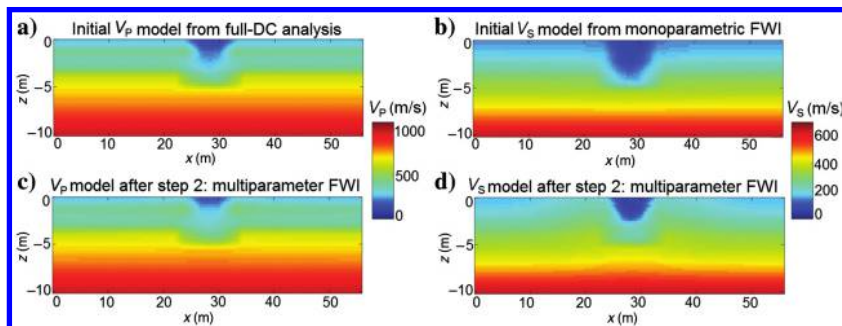

Figure 23. Vertical 2D sections (crossing the target's center) of the 3D velocity models, synthetic application. (a) Initial V_P model from full-DC analysis. (b) Initial V_S model after monoparametric FWI. (c) Final V_P model after multiparameter FWI. (d) Final V_S model after multiparameter FWI.
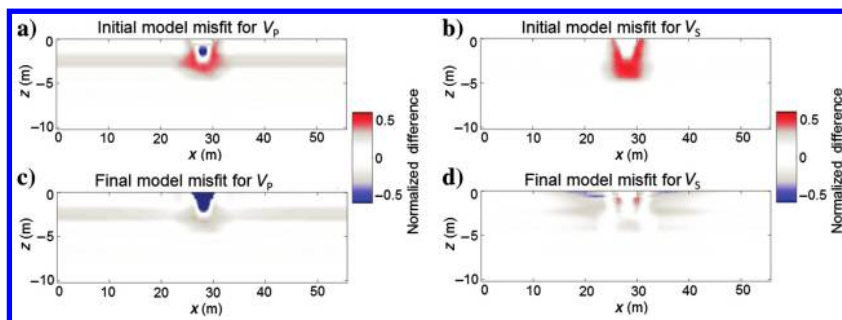

Figure 24. Vertical 2D sections (crossing the target's center) of the 3D model misfit: (a) (Reference V_P model – initial V_P model from DC)/reference V_P model. (b) (Reference V_S model – initial V_S model from monoparametric FWI)/reference V_S model. (c) (Reference V_P model – final V_P model from multiparameter FWI)/reference V_P model. (d) (Reference V_S model – final V_S model from multiparameter FWI)/reference V_S model.

model-oriented strategy, using the synthetic data set and a 2D acquisition layout. The strategy consists of two sequential steps: monoparametric FWI (with respect to V_S) followed by multiparameter ($V_P + V_S$) FWI. In the preliminary step, the initial V_P model from SWs analysis (Figure 23a) is kept invariable.

Figure 23b shows the V_S model obtained after the monoparametric FWI step. Figure 23c and 23d shows the models obtained after the multiparameter FWI, and Figure 24 shows the related model misfits. After the monoparametric FWI, the V_S model improves only down to 2 m (Figures 23b and 24d). On the contrary, after the multiparameter FWI, whereas the V_P model does not improve significantly (as expected), the V_S model's resolution improves remarkably, delineating the target boundaries at the deepest region (Figures 23d and 24d). Nevertheless, the success of this strategy might be case-dependent, and it may not work properly in the presence of complex topography. However, when irregular topography is present, the lateral velocity variations cause backscattered SWs and conversion to higher modes. Thus, the topography effects should be considered in the modeling engine. Moreover, SWs propagation under a complex topography, generating secondary BWs, may help for the illumination of the deeper part of the model.

Attenuation and density

Another aspect that requires analysis is the effect of variable density and attenuation in FWI. In this study, they are assumed constant and are fixed during the inversion. The choice of a constant density was aimed at focusing the analysis on the velocity model update while avoiding the additional trade-off introduced when FWI aims at reconstructing simultaneously the velocity and density. As far as attenuation is concerned, because its implementation in the FWI tool relies on a constant SLS mechanism over a limited frequency band, the use of a constant value for the Q parameter should not influence the results significantly. This fact is justified by the relatively limited frequency band used in this study for FWI (3–40 Hz) and the relatively low number of propagated wavelengths (nearly four wavelengths over a maximum offset of approximately 25 m). Certainly, the presence of higher frequencies may require a better representation of the Q values. In any case, because the Q factor is important for appropriate modeling of the AVO, more accurate FWI results would be expected when using variable (and correct) values for the attenuation factor. Apart from the proper amplitude representation of the modeled data, the use of an accurate value for the Q factor may also control the proper estimation of the real source wavelet while avoiding additional corrections (e.g., Groos et al., 2014).

CONCLUSION

We proposed an integrated workflow, based on 2D SW analysis and 3D FWI, to enhance the resolution in the imaging of sharp-interface shallow targets. We performed tests on a well-known real

target, represented by a loose-sand body embedded in more compact sediments. In this context, seismic data are dominated by complex-scattered and highly energetic SWs, making the application of FWI a challenging task. Additional challenges for FWI are created by the flat topography of the investigated area, which facilitates the SWs' forward-scattering regime, whereas FWI is mainly based on a back-scattering one (BWs). The presence of irregular topography would have better fulfilled the engine behind FWI because it would have generated secondary BWs and SWs with higher modes of propagation, but it would have rendered the SWs' fundamental mode indi-viduation more challenging.

We built different initial models, laterally homogeneous and hetero-geneous, using SW analysis procedures. A relatively simple 3D elastic FWI workflow, applied to synthetic and field data, overall improved the resolution of the initial models. QC and data misfit analysis show that the best FWI results are obtained using laterally variable initial models. The final data fitting is accurate for the near-offset traces and in correspondence to the target, whereas the fitting of some far-offset arrivals and backscattered phases requires the use of a 3D acquisition layout or different FWI strategies.

A 3D acquisition layout, with a 3D distribution of the sources around the low-velocity target, ensured a more accurate reconstruction of the target's boundaries and lateral extension, for synthetic and field data application. Adopting a 3D acquisition scheme guaranteed a better fitting of the far-offset arrivals and backscattered phases. Better FWI results were obtained, again, when using the initial models retrieved by full-DC analysis. However, the initial models built from single-DC analysis also allowed for an accurate reconstruction of the target's shape and lateral extension, except for the presence of some artifacts in the final models.

ACKNOWLEDGMENTS

DATA AND MATERIALS AVAILABILITY

Data associated with this research are available and can be obtained by contacting the corresponding author.

REFERENCES

Amrouche, M., and H. Yamanaka, 2015, Two-dimensional shallow soil profiling using time-domain waveform inversion: Geophysics, **80**, no. 1, EN27–EN41, doi: 10.1190/geo2014-0027.1.

Athanasopoulos, N., E. Manukyan, T. Bohlen, and H. Maurer, 2018, Accurate reconstruction of shallow P-wave velocity model with time-windowed elastic full-waveform inversion: 80th Annual International Conference and Exhibition, EAGE, Extended Abstracts, We_P8_12, doi: 10.3997/2214-4609.201801305.

Bergamo, P., D. Boiero, and L. V. Socco, 2012, Retrieving 2D structures from surface-waves data by means of space-varying windowing: Geophysics, **77**, no. 4, EN39–EN51, doi: 10.1190/geo2012-0031.1.

Borisov, D., F. Gao, P. Williamson, and J. Tromp, 2020, Application of 2D full-waveform inversion on exploration land data: Geophysics, **85**, no. 2, R75–R86, doi: 10.1190/geo2019-0082.1.

Borisov, D., R. Modrak, F. Gao, and J. Tromp, 2018, 3D elastic full-waveform inversion of surface waves in presence of irregular topography using an envelope-based misfit function: Geophysics, **83**, no. 1, R1–R11, doi: 10.1190/geo2017-0081.1.

Borisov, D., and S. C. Singh, 2015, Three-dimensional elastic full waveform inversion in a marine environment using multicomponent ocean-bottom cables: A synthetic study: Geophysical Journal International, **201**, 1215–1234, doi: 10.1093/gji/ggv048.

Bretaudeau, F., R. Brossier, D. Leparoux, O. Abraham, and J. Virieux, 2013, 2D elastic full-waveform imaging of the near surface: Application to synthetic and a physical modeling data set: Near Surface Geophysics, **11**, 307–316, doi: 10.3997/1873-0604.2012067.

Brossier, R., S. Operto, and J. Virieux, 2009, Seismic imaging of complex onshore structures by 2D elastic frequency domain full-waveform inversion: Geophysics, **74**, no. 6, WCC63–WCC76, doi: 10.1190/1.3215771.

Brossier, R., S. Operto, and J. Virieux, 2010, Which data residual norm for robust elastic frequency-domain full waveform inversion?: Geophysics, **75**, no. 3, R37–R46, doi: 10.1190/1.3379323.

Bunks, C., F. M. Salek, S. Zaleski, and G. Chavent, 1995, Multiscale seismic waveform inversion: Geophysics, **60**, 1457–1473, doi: 10.1190/1.1443880.

Butzer, S., A. Kurzmann, and T. Bohlen, 2013, 3D elastic full-waveform inversion of small-scale heterogeneities in transmission geometry: Geophysical Prospecting, **61**, 1238–1251, doi: 10.1111/1365-2478.12065.

Dou, S., and J. B. Ajo-Franklin, 2014, Full-wavefield inversion of surface waves for mapping embedded low-velocity zones in permafrost: Geophysics, **79**, no. 6, EN107–EN124, doi: 10.1190/geo2013-0427.1.

Epanomeritakis, I., V. Akçelik, O. Ghattas, and J. Bielak, 2008, A Newton-CG method for large-scale three-dimensional elastic full waveform seismic inversion: Inverse Problems, **24**, 034015–26, doi: 10.1088/0266-5611/24/3/034015.

Fathi, A., L. Kallivokas, and B. Poursartip, 2015, Full waveform inversion in three-dimensional PML-truncated elastic media: Computer Methods in Applied Mechanics and Engineering, **296**, 39–72, doi: 10.1016/j.cma.2015.07.008.

Fathi, A., B. Poursartip, K. H. Stokoe, and L. Kallivokas, 2016, Three dimensional P- and S-wave velocity profiling of geotechnical sites using full-waveform inversion driven by field data: Soil Dynamics and Earthquake Engineering, **87**, 63–81, doi: 10.1016/j.soildyn.2016.04.010.

Fichtner, A., 2011, Full seismic waveform modeling and inversion: Springer Science & Business Media.

Fichtner, A., J. Trampert, P. Cupillard, E. Saygin, T. Taymaz, Y. Capdeville, and A. V. Nor, 2013, Multiscale full waveform inversion: Geophysical Journal International, **194**, 534–556, doi: 10.1093/gji/ggt118.

Groos, L., M. Schäfer, T. Forbriger, and T. Bohlen, 2014, The role of attenuation in 2D full-waveform inversion of shallow-seismic body and Rayleigh waves: Geophysics, **79**, no. 6, R247–R261, doi: 10.1190/geo2013-0462.1.

Groos, L., M. Schäfer, T. Forbriger, and T. Bohlen, 2017, Application of a complete workflow for 2D elastic full-waveform inversion to recorded shallow-seismic Rayleigh waves: Geophysics, **82**, no. 2, R109–R117, doi: 10.1190/geo2016-0284.1.

Hauksson, E., and P. M. Shearer, 2006, Attenuation models (Q_p and Q_s) in three dimensions of the southern California crust: Inferred fluid saturation at seismogenic depths: Journal of Geophysical Research, **111**, B05302, doi: 10.1029/2005JB003947.

He, W., R. Brossier, L. Metivier, and J. Virieux, 2018, A practical work-flow of full waveform inversion to process land seismic data: Synthetic study: 80th Annual International Conference and Exhibition, EAGE, Extended Abstracts, Th_A12_04, doi: 10.3997/2214-4609.201801376.

Irnaka, T. M., R. Brossier, L. Métivier, T. Bohlen, and Y. Pan, 2019, Towards 3D 9C elastic full waveform inversion of shallow seismic wavefields — Case study Ettlingen line: 81st Annual International Conference and Exhibition, EAGE, Extended Abstracts, We_P01_04, doi: 10.3997/2214-4609.201900994.

Khosro Anjom, F., D. Teodor, C. Comina, R. Brossier, J. Virieux, and L. V. Socco, 2019, Full waveform matching of VP and VS models from surface waves: Geophysical Journal International, **218**, 1873–1891, doi: 10.1093/gji/ggz279.

Köhn, D., T. Meier, M. Fehr, D. De Nil, and M. Auras, 2016, Application of 2D elastic Rayleigh waveform inversion to ultrasonic laboratory and field data: Near Surface Geophysics, **14**, 461–467, doi: 10.3997/1873-0604.2016027.

Komatitsch, D., and J. Tromp, 1999, Introduction to the spectral element method for three-dimensional seismic wave propagation: Geophysical Journal International, **139**, 806–822, doi: 10.1046/j.1365-246x.1999.00967.x.

Krampe, V., Y. Pan, and T. Bohlen, 2019, Two-dimensional elastic full-waveform inversion of Love waves in shallow vertically transversely isotropic media: Synthetic reconstruction tests: Near Surface Geophysics, **17**, 449–461, doi: 10.1002/nsg.12061.

Lailly, P., 1983, The seismic inverse problem as a sequence of before stack migrations: Conference of Inverse Scattering: Theory and Application, Society of Industrial and Applied Mathematics (SIAM).

Masoni, I., J.-L. Boelle, R. Brossier, and J. Virieux, 2016, Layer stripping FWI for surface waves: 86th Annual International Meeting, SEG, Expanded Abstracts, 1369–1373, doi: 10.1190/segam2016-13859781.1.

Masoni, I., R. Brossier, J.-L. Boelle, M. Macquet, and J. Virieux, 2014, Robust full-waveform inversion of surface waves: Seismic Technology, **11**, 1126–1130.

Métivier, L., and R. Brossier, 2016, The seiscope optimization toolbox: A large-scale non-linear optimization library based on reverse communication: Geophysics, **81**, no. 2, F11–F25, doi: 10.1190/geo2015-0031.1.

Nguyen, T. D., and K. T. Tran, 2018, Site characterization with 3D elastic full-waveform tomography: Geophysics, **83**, no. 5, R389–R400, doi: 10.1190/geo2017-0571.1.

Nocedal, J., and S. J. Wright, 2006, Numerical optimization, 2nd ed.: Springer.

Nuber, A., E. Manukyan, and H. Maurer, 2016, Enhancement of near surface elastic full waveform inversion results in regions of low sensitivities: Journal of Applied Geophysics, **122**, 192–201, doi: 10.1016/j.jappgeo.2015.09.020.

Operto, S., A. Miniussi, R. Brossier, L. Combe, L. Métivier, V. Monteiller, A. Ribodetti, and J. Virieux, 2015, Efficient 3-D frequency-domain mono-parameter full-waveform inversion of ocean-bottom cable data: Application to Valhall in the visco-acoustic vertical transverse isotropic approximation: Geophysical Journal International, **202**, 1362–1391, doi: 10.1093/gji/ggv226.

Pan, Y., L. Gao, and T. Bohlen, 2019, High-resolution characterization of near-surface structures by surface wave inversions: From dispersion curve to full waveform: Survey in Geophysics, **40**, 167–195, doi: 10.1007/s10712-019-09508-0.

Pan, Y., J. Xia, Y. Xu, L. Gao, and Z. Xu, 2016, Love-wave waveform inversion in time domain for shallow shear-wave velocity: Geophysics, **81**, no. 1, R1–R14, doi: 10.1190/geo2014-0225.1.

Plessix, R. E., 2006. A review of the adjoint-state method for computing the gradient of a functional with geophysical applications: Geophysical Journal International, **167**, 495–503, doi: 10.1111/j.1365-246X.2006.02978.x.

Pratt, R. G., 1999, Seismic waveform inversion in the frequency domain — Part 1: Theory and verification in a physical scale model: Geophysics, **64**, 888–901, doi: 10.1190/1.1444597.

Romdhane, A., G. Grandjean, R. Brossier, F. Réjiba, S. Operto, and J. Virieux, 2011, Shallow structures characterization by 2D elastic waveform inversion: Geophysics, **76**, no. 3, R81–R93, doi: 10.1190/1.3569798.

Schäfer, M., L. Groos, T. Forbriger, and T. Bohlen, 2014, Line-source simulation for shallow-seismic data — Part 2: Full-waveform inversion — A synthetic 2-D case study: Geophysical Journal International, **198**, 1405–1418, doi: 10.1093/gji/ggu171.

Shi, T., J. Zhang, Z. Huang, and C. Jin, 2015, A layer-stripping method for 3D near-surface velocity model building using seismic first-arrival times: Journal of Earth Sciences, **26**, 502–507.

Sirgue, L., O. I. Barkved, J. Dellinger, J. Etgen, U. Abertin, and J. H. Kommedal, 2010, Full-waveform inversion: The next leap forward in imaging at Valhall: First Break, **28**, 65–70, doi: 10.3997/1365-2397.2010012.

Smith, J. A., D. Borisov, H. Cudney, R. D. Miller, R. Modrak, M. Moran, S. L. Peterie, S. D. Sloan, J. Tromp, and Y. Wang, 2019, Tunnel detection at Yuma Proving Ground, Arizona, USA — Part 2: 3D full-waveform inversion experiments: Geophysics, **84**, no. 1, B101–B120, doi: 10.1190/geo2018-0599.1.

Socco, L. V., and D. Boiero, 2008, Improved Monte Carlo inversion of surface wave data: Geophysical Prospecting, **56**, 357–371, doi: 10.1111/j.1365-2478.2007.00678.x.

Socco, L. V., and C. Comina, 2017, Time-average velocity estimation through surface-wave analysis — Part 2: P-wave velocity: Geophysics, **82**, no. 3, U61–U73, doi: 10.1190/geo2016-0368.1.

Socco, L. V., C. Comina, and F. Khosro Anjom, 2017, Time-average velocity estimation through surface-wave analysis — Part 1: S-wave velocity: Geophysics, **82**, no. 3, U49–U59, doi: 10.1190/geo2016-0367.1.

Tarantola, A., 1984, Linearized inversion of seismic reflection data: Geophysics Prospecting, **32**, 998–1015.

Teodor, D., C. Comina, F. Khosro Anjom, L. V. Socco, J. Virieux, P.-T. Trinh, and R. Brossier, 2018, Building initial models for full-waveform inversion of shallow targets by surface waves dispersion curves clustering

and data transform: 88th Annual International Meeting, SEG, Expanded Abstracts, 4738–4742, doi: 10.1190/segam2018-2997848.1

Teodor, D., C. Comina, L. V. Socco, F. Khosro Anjom, J. Virieux, R. Brossier, and P. T. Trinh, 2019, Elastic full waveform inversion tests for shallow targets reconstruction from surface waves analysis based initial models: 81st Annual International Conference and Exhibition, EAGE, Extended Abstracts, Tu_R16_13, doi: 10.3997/2214-4609.201900976

Tran, K. T., and D. R. Hiltunen, 2012a, One-dimensional inversion of full waveform using genetic algorithm: Journal of Environmental and Engineering Geophysics, **17**, 197–213, doi: 10.2113/JEEG17.4.197.

Tran, K. T., and D. R. Hiltunen, 2012b, Two-dimensional inversion of full waveform using simulated annealing: Journal of Geotechnical and Geo-environmental Engineering, **138**, 1075–1090, doi: 10.1061/(ASCE)GT.1943-5606.0000685.

Tran, K. T., and M. McVay, 2012, Site characterization using Gauss-Newton inversion of 2-D full seismic waveform in time domain: Soil Dynamics and Earthquake Engineering, **43**, 16–24, doi: 10.1016/j.soildyn.2012.07.004.

Tran, K. T., M. Mirzanejad, M. McVay, and D. Horhota, 2019, 3-D time-domain Gauss-Newton full waveform inversion for near-surface site characterization: Geophysical Journal International, **217**, 206–218, doi: 10.1093/gji/ggz020.

Trinh, P. T., R. Brossier, L. Métivier, L. Tavard, and J. Virieux, 2018, Data-windowing hierarchy in multi-parameter elastic FWI: 3D synthetic foot-hills case study: 80th Annual International Conference and Exhibition, EAGE, Extended Abstracts, Th_P3_11, doi: 10.3997/2214-4609.201801570.

Trinh, P. T., R. Brossier, L. Metivier, L. Tavard, and J. Virieux, 2019, Efficient time-domain 3D elastic and visco-elastic FWI using a spectral-element method on flexible Cartesian-based mesh: Geophysics, **84**, no. 1, R75–R97, doi: 10.1190/geo2018-0059.1.

Trinh, P. T., R. Brossier, L. Métivier, J. Virieux, and P. Wellington, 2017, Bessel smoothing filter for spectral element mesh: Geophysical Journal International, **209**, 1489–1512, doi: 10.1093/gji/ggx103.

Vigh, D., K. Jiao, D. Watts, and D. Sun, 2014, Elastic full-waveform inversion application using multicomponent measurements of seismic data collection: Geophysics, **79**, no. 2, R63–R77, doi: 10.1190/geo2013-0055.1.

Virieux, J., and S. Operto, 2009, An overview of full waveform inversion in exploration geophysics: Geophysics, **74**, no. 6, WCC1–WCC26, doi: 10.1190/1.3238367.

Wang, Y., R. D. Miller, S. L. Peterie, S. D. Sloan, M. L. Moran, H. H. Cudney, J. A. Smith, D. Borisov, R. Modrak, and J. Tromp, 2019, Tunnel detection at Yuma Proving Ground, Arizona, USA — Part 1: 2D full-waveform inversion experiment: Geophysics, **84**, no. 1, B95–B105, doi: 10.1190/geo2018-0598.1.

Warner, M., A. Ratcliffe, T. Nangoo, J. Morgan, A. Umpleby, N. Shan, V. Vinje, I. Stekl, L. Guash, C. Win, G. Conroy, and A. Bertrand, 2013, Anisotropic 3D full-waveform inversion: Geophysics, **78**, no. 2, R59–R80, doi: 10.1190/geo2012-0338.1.

Xing, Z., and A. Mazzotti, 2019a, Two-grid full-waveform Rayleigh-wave inversion via a genetic algorithm — Part 1: Method and synthetic examples: Geophysics, **84**, no. 5, R805–R814, doi: 10.1190/geo2018-0799.1.

Xing, Z., and A. Mazzotti, 2019b, Two-grid full-waveform Rayleigh-wave inversion via a genetic algorithm — Part 2: Application to two actual data sets: Geophysics, **84**, no. 5, R815–R825, doi: 10.1190/geo2018-0800.1.

Yang, P., R. Brossier, L. Métivier, and J. Virieux, 2016a, A review on the systematic formulation of 3D multiparameter full waveform inversion in viscoelastic medium: Geophysical Journal International, **207**, 129–149, doi: 10.1093/gji/ggw262.

Yang, P., R. Brossier, L. Métivier, and J. Virieux, 2016b, Wavefield reconstruction in attenuating media: A checkpoint-assisted reverse-forward simulation method: Geophysics, **81**, no. 6, R349–R362, doi: 10.1190/geo2016-0082.1.

Yang, P., R. Brossier, and J. Virieux, 2016c, Wavefield reconstruction from significantly decimated boundaries: Geophysics, **81**, no. 5, T197–T209, doi: 10.1190/geo2015-0711.1.

Biographies and photographs of the authors are not available.

This article has been cited by:

1. Fatemeh Pourahmadian, Kevish Napal. 2022. Poroelastic near-field inverse scattering. *Journal of Computational Physics* **455**, 111005. [Crossref]

2. A. Arato, F. Vagnon, C. Comina. 2022. First application of a new seismo-electric streamer for combined resistivity and seismic measurements along linearly extended earth structures. *Near Surface Geophysics* **20**:2, 117-134. [Crossref]

3. Utku Harmankaya, Ayse Kaslilar. 2022. Modelling 3D elastodynamic wave scattering due to density and Lamé parameter contrasts of near-surface scatterers. *Near Surface Geophysics* **134**. . [Crossref]